International Journal of Thermofluid Science and Technology (2021)
Volume 8, Issue 4, Paper No. 080402
https://doi.org/10.36963/IJTST.2021080402
Research Article

Optimization of Electrical and Optical Properties of Indium Tin Oxide Thin Films Prepared by Magnetron Sputtering

Muslimin[1], Darsikin[2], Marungkil Pasaribu[3], Nurulhuda Rahman[4]

[1,2,3] *Dept. of Physics education, Tadulako University, Central Sulawesi, 94119, Indonesia*
[4] *Dept. of Agribusiness, Tadulako University, Central Sulawesi, 94119, Indonesia*

ARTICLE INFO

Received: 18 May 2021; Received in revised form: 18 Sept. 2021; Accepted: 28 Sept. 2021; Published online 10 Oct. 2021

Keywords :

Oxygen partial pressure
Annealing
Structure
Elektrical and optical properties

ABSTRACT

Indium tin oxide (ITO) is one of the most interesting physical properties to be studied. The ITO material properties depend heavily on deposition techniques and post deposition treatment. The deposition of the ITO thin film was performed by dc sputtering by changing the partial oxygen pressure at the time of deposition and the different annealing temperature to the sample. The X-ray result obtained all the samples having maximal orientation of plane (400). The result of structural analysis obtained by the latice constante (10,17-10,25) Å, and the big grain (109,10-122,81) nm, Latice constante and big grain have changed each sample towards smaller if partial pressure of oxygen and annealing temperature the higher. The electrical resistivity, density, mobility and band gap changes if the partial pressure of oxygen and the annealing temperature are increased. Density (2.77-6.89) x 10^{20} cm^{-3}, mobility (19,63-32,98) $cm^2V^{-1}s^{-1}$, band gap (3.78-4.30) eV and resistivity (3.67-9.7) x 10^{-4} cm^{-3}, the lowest resistivity was obtained at 3.70% oxygen partial pressure and 250 ^oC annealing temperature. Optical cultures also experienced changes including refractive index (2.09-2.25), constuction damping (2.93-3.49), absorption coefficient (0.036-0.072) and transmittance (81.94%-87.12%). The highest transmittance is obtained at an oxygen partial pressure of 8.90% with an annealing temperature of 250 °C.

@ Published at www.ijtf.org

1. Introduction

The electrical properties of the thin film In_2O_3: SnO_2 (indium tin oxide) or more known by the name ITO is highly dependent on the deposition parameters and the degree of crystallinity of the formed layer [1, 2]. The degree of oxygen deprivation at the time of deposition may affect Sn dopping on the crystals that are formed. Dopping Sn as a donor will replace so it will be a source of extrinsic charge. There are two important things that contribute to the free charge on the ITO thin layer that forms the oxygen vacuum and substitution of the Sn atom against the In atom [3]. The oxygen vacuum will produce two free electrons and substitution of Sn atom on the In atom will result in a free electron [4, 5].

Corresponding e-mail: fisikamuslim@gmail.com (Muslimin)

A thin films of oxygen-depleted ITO will form a group consisting of the arrangement of free atoms In and Sn as well as black oxide InO and SnO The formation of black oxide groups in the ITO thin films may result in the layer becoming less transparent [6, 7]. The amorphous layer of ITO will crystallize quickly at a temperature of 150 °C followed by electronic structure changes when it is temperature at 135 °C [8, 9]. The magnitude of the grains will increase with the rise of annealing temperature.

The electrical and optical properties of ITO are highly dependent on high levels of crystallinity [10, 11]. The lack of oxygen prior to loading is due to the fact that at the time of deposition, the oxygen of the In_2O_3 and SnO_2 compounds are first deposited because the boiling point of the oxygen is smaller than the boiling point In and Sn as a result of oxygen deficiency.

Lack of oxygen during the deposition process can cause In atoms and Sn atoms to be completely oxidized. These events will affect the structure, electrical properties and optic thin films that are formed [12, 13]. The addition of oxygen from the outside during the deposition process can join the Atoms and Sn atoms forming the oxide compound. Atoms In and Sn that are electrically inactive at the insertion position, can be activated by annealing [14].

The electrical properties and optical properties of the ITO thin film depend on the amount of doping Sn against In and the rate of oxygen deprivation in In_2O_3 [15–17]. The structure, electrical and optical properties of ITO can be optimized by altering the deposition parameters such as the oxygen partial pressure, and annealing to change the density of the load carrier and charge carrier mobility [18, 19]. Therefore, the addition of oxygen at deposition, and annealing is one way that is considered effective in increasing the density and mobility of the load on the ITO thin films. Partial oxygen pressure can determine the degree of ITO layer transmit the energy band shift occurring on the absorption curve can be attributed to the change in the number of vacant oxygen in the formed thin films [20].

2. Experiments

The ITO thin films is made by using dc sputtering PK 75 with rotary trivac D 665 B and 1000 rotary pump, 1000/1500 turbotonic coverer frequencies such as **Fig. 1**. Samples were analyzed from XRD and UV-Vis-NIR results, Hall Effect, four point probes.

Deposition was performed with some optimization is percentage of partial pressure of oxygen and annealing after deposition. The deposition is carried out in the vacuum chamber of 10^{-5} mBarr pressure, the sputtering process begins, at the same time the argon gas and oxygen gas are fed through the flow meter until the pressure reaches 2 x 10^{-3} mBarr. The partial pressure of oxygen that is introduced in each deposition is the ratio of the argon gas pressure with the oxygen gas of each sample of 2.50%, 3.70%, 5.10%, 6.15% and 8.9%, respectively. Annealing was carried out in a vacuum chamber at a pressure of 10^{-3} mBarr for 60 minute with a temperature of 175 ^oC and 250 ^oC in each sample.

Thin films thickness was calculated based on the reflectance measurements of the UV-Vis results at wavelength (350 - 800) nm. The microstructure analysis was performed by Philips Analitical Difractometer PW 3710 x-ray diffractometer with anode tube Co. The width of the diffraction angle (2θ) is 200-700, the peak position in degrees and the Full Width at Half Maximum (FWHM) known as the indicator. The size of the crystals, lattice distortion, grain size and lattice constants were obtained from XRD results.

Measurement The electrical properties were analyzed by four point probes as in **Fig. 2**. Carrier concentration, charge carrier mobility and band gap are obtained by using some equations. Measurements of the ITO optical properties used UV-Vis, reflectance, transmittance, constants attenuation and

absorption were obtained using some equations from UV-Vis results.

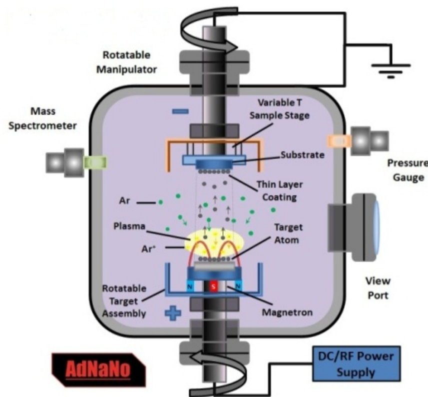

Fig.1. dc sputtering instrument.

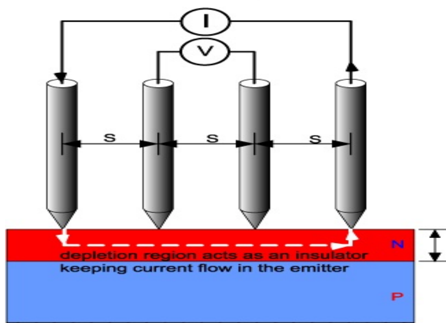

Fig. 2. Four-point probes instrument.

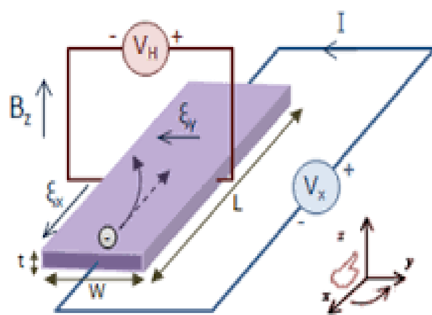

Fig. 3. Hall effect measurement.

The measurement of the ITO crystal micro structure is characterized by x-ray diffraction primarily for grain size, lattice constants and crystal orientation. The obtained crystals have orientation orientation) hkl plane (400) **Fig 4**. The calculation of the grain size **G** and the lattice constants is done at the maximum orientation angle of 2θ about 40.9°.

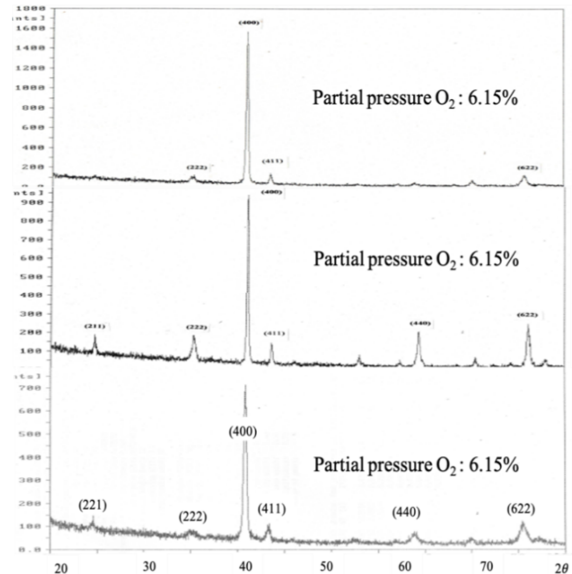

Fig. 4. x-ray diffraction patterns of ITO film for different partialoxygen pressure.

The resulting pattern of XRD ITO coatings is crystal with a tendency to have a field orientation (400). The orientation of the diffraction coating plates is the same for all variations in oxygen content, indicating considerable compatibility with In_2O_3 bulk cube structure data [21]. The greatest intensity is at the corner (2θ) 40.9° which is owned by the field reflection (400) of the bcc body centered cubic (bcc) structure. The field intensity (400) and (222) stand out against the background intensity so as to imply that the material structure is already crystallized by the smaller FWHM. It is estimated that the shape of this diffraction pattern is due to the deposition temperature of this material leaving the amorphous region.

In the XRD pattern indicates maximum intensity in the (400) plane there is a tendency for increasing oxygen levels. The increasing intensity of the diffraction pattern and the diminution of FWHM occurs due to the increase in oxygen vacancy concentration and the diffusion rate due to annealing in the deposited layer. The change is due to the In-free atom and the Sn impurities decreasing as it is oxidized by the oxygen introduced at the time of deposition. Oxygen from In_2O_3 and

Sn_2O compounds is firstly deposited because the boiling point of oxygen is less than the boiling point of In and Sn due to oxygen deficiency.

The intensity of the diffraction pattern there is an increasing tendency and full width at half maksimum (FWHM) in samples being annealing temperature 250°C intensity and maximum half peak. In line with that done by [22], it obtains a peak in the field (222) having maximum intensity, with the orientation of the plating 400 (26), and the plane 400 at the deposition temperature 350 °C by the Beam electron method whereas with HDPE in the (222) field it is explained that the amorphous indium oxide will generally crystallize rapidly at a temperature of 150 °C.

In general, the widening of the peak x-ray diffraction pattern of a crystal sample is affected by the size of the crystal and the mictrostrain effect [23, 24]. The diffraction peak width is assumed as a result of small size and not due to lattice strain.

The crystallite size was calculated from the XRD pattern using formula Debye-Scherrer [25]

$$G = \frac{0.9\ \lambda}{\beta^{\cos\theta}} \quad (1)$$

where λ is x-ray wave length , β is FWHM in radian and θ is Bragg's angle.

The change in grain size is due to the oxygen vacancy rate and the diffusion rate due to the annealing temperature. The entire layer will be perfectly crystallized into fine grains of size (68.99-122,76) nm. This average size will increase to 112.09 nm for annealing temperatures of 175 °C and 117.06 for annealing 250 °C. The change in crystal grain size at (175-250) °C temperature due to annealing has almost not changed significantly since the free atoms are almost all experiencing diffusion.

The results obtained therefrom the results of indium amorphous oxide will generally crystallize rapidly at a temperature of 150 °C, because crystallization continues, the entire layer is filled with granules and almost perpendicular to the surface [26, 27]. Annealing temperatures can make the crystals grow larger and reach the surface so that they touch each other on the surface and leave the amorphous area [28].

The grain size is almost the same as that obtained by [29] with (100-460) nm at temperature (423-473) K and with (35-50) nm which is carried out at 350°C with 5% by weight of Sn. The lattice constants obtained 11,9 nm, substrate temperature 600°C [30].

Conversion of lattice constants can be analyzed using the Cohen method [31]:

$$\frac{\Delta d}{d} = \frac{\Delta a}{a} = \kappa cos\ \theta \quad (2)$$

$$d_{hkl} = \frac{a}{\sqrt{h^2 + k^2 + l^2}} \quad (3)$$

Where is size lattice, **a** is lattice constant, κ is constant 0,9 and hkl is prefared orientation.

Constante lattice smallest 10.17 Å on oxygen partial prssure 6.15% annealing 175 °C. The result of lattice analysis has distortion of lattice both shrinkage and widening due to the influence of oxygen partial prssure and temperature annealing. The lattice constants of the above samples are quite good when compared to the ITO price of the ASTM card of 10.118 Å. The price of shrinkage of grating parameters obtained is quite good because it is relatively small that is about (0.052 - 0.212) Å.

Table 1. Structural parameter of prepared ITO thin films for different partial oxygen and annealing

Oxygen partial (%)	Annealing (°C)	2θ(deg)	Intensity max	FWHM (deg)	hkl	Latice constant (Å)	Grain (hkl) (nm)
2.50	175	41.065	400	0.16	400	10.25	122.81
	250	40.955	729	0.16	400	10.23	122.76
3.70	175	40.880	745	0.18	400	10.24	109.44
	250	41.250	686	0.16	400	10.21	122.80
5.10	175	41.060	729	0.18	400	10.21	109.51
	250	40.910	226	0.18	400	10.21	109.10
6.15	175	41.180	325	0.18	400	10.17	109.55
	250	35.345	350	0.16	222	10.19	120.70
8.90	175	41.060	747	0.18	400	10.20	109.16
	250	41.135	1102	0.18	400	10.21	109.95

Constant crystal lattice changes there is a downward trend if oxygen partial pressure is increasing [32–34]. This change has something to do with the distortion occurring in the crystal caused by the point defect caused by the oxygen atom as a relatively small sized insert compared with the In and Sn radius of about 1.509 Å [35]. This local distortion acts as an additional scattering center to the electron current flowing through the crystal to produce resistance to the crystal.

The lattice constuction changes due to strains, due to the contribution of oxygen vacancies, the effects of oxygen partial pressure at the time of deposition is very significant with the consteous change of lattice while the lattice contant becomes decreased as the temperature rises annealing is caused by Sn/In getting smaller [36, 37]. Decrease in lattice contents of microstrain effect, and elastic strain caused by impurity, vacancy [38], [39]. Results analysis of ITO thin films structures such as Table 1.

3.2 Electrical Studies

Indium Tin Oxide is a compound doped with Sn. Atom dopping Sn can function as a substitute for one of the atoms of the master In_2O k crystal also can place itself in the insertion position. Sn atoms can also form a bond with oxygen such as SnO or SnO_2 based on the valence of +2 or +4 [40 – 42]. The $Sn+^4$ state of SnO_2 can function as an n-type donor releasing electrons in the conduction energy band.

The concentration of atom dopping Sn increases then the electron wave function at the level of impurities will overlap each other. The occurrence of this overlapping effect on the potential changes in the energy levels of each electron resulting in the formation of a band of energy levels in the area. The impurity band of energy will widen and merge into one with an intrinsic band if the concentration of impurities continues to increase.

Another effect that arises as a consequence of the increase in impurity concentration is the formation of impurity energy bands that can affect the energy bands. This impedance causes the lower energy band to expand, resulting in a narrow band of energy bands (tail band effect).

Price estimates of critical density donors can be determined by criteria n Moott that is , $n_c^{\frac{1}{3}} a_o^* \approx 0{,}25$, $a_0^* = \frac{h^2 \varepsilon_0 \varepsilon^M}{\pi\, e^2 m_c^*}$, ε^M static dielectric constants of the parent grid ($\varepsilon^M = \varepsilon^{In_2O_3}$ ($\varpi = 0$) = 8,9). effective mass on the conduction band ($m_c^* = 0{,}35\ m_e$) with a Bohr radius $a_0^* \approx 1{,}3$ nm [40].

Table 2. Electrical parameter ITO thin films for different oxygen partial and annealing

Oxygen partial (%)	Annealing (°C)	Resistivity ($x10^{-4}$ cm^{-3})	Density (n) $x10^{20}$ cm^{-3}	Mobility (μ) ($cm^2V^{-1}s^{-1}$)	Energy Gap (eV)
2.50	175	5.50	5.39	21.49	3.92
	250	3.67	6.03	28.24	3.81
3.70	175	4.89	6.51	19.63	4.29
	250	3.06	6.89	29.64	3.92
5.10	175	7.34	3.38	25.19	4.20
	250	4.89	3.88	32.94	3.78
6.15	175	9.17	3.05	22.35	4.30
	250	6.11	3.25	31.47	4.10
8.90	175	9.78	2.77	22.86	4.35
	250	6.72	2.82	32.98	4.20

The structure of the energy band of indium tin oxide with high dopping density is shown,

$$E_c(k) = E_c^0 + \hbar\Sigma_c(k) \quad (4)$$

$$E_v(k) = E_v^0 + \hbar\,\Sigma_v(k)$$

$E_v(k)$ with dopping valence energy and E_c (k) dopping conduction energy

The density and mobility of electron carriers of extrinsic semiconductor loads due to electrons [43],

$$\mu = \left(\frac{4e}{h}\right)\left(\frac{\pi}{3}\right)^{1/3} n^{-2/3} \quad (5)$$

μ is the carrier mobility, n electron density. The electrical conductivity σ can be expressed by equation,

$$\sigma = e(\mu_n n + \mu_h p) = \frac{1}{\rho} \quad (6)$$

with σ electrical conductivity, ρ electrical resistivity.

Thin films resistivity to oxygen partial pressure and annealing such as **Fig. 5**. The lowest ITO thin film resistivity was obtained at a partial oxygen pressure of 3.7% by annealing treatment at a temperature of 250 °C. This resistivity is related to the load carrier density obtained which is 6.89 x 10^{20} cm^{-3} with a charge carrier mobility of 29.64 cm^2/Vdet with a band gap of 3.92 eV.

ITO thin films made at the same oxygen partial pressure but different annealing treatments will produce different resistivities. Meanwhile, the resistivity of the ITO thin layer made at 3.7% oxygen partial pressure with annealing at a temperature of 175 °C was higher than that of the thin film annealed at 250 °C.

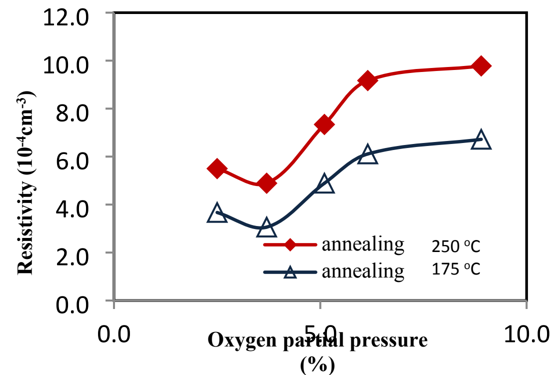

Fig. 5. Risistivity to oxygen and annealing.

This is related to the level of crystallinity. This can be seen with the smaller carrier density obtained, namely 4.86 x 10^{20} cm^{-3} and mobility 34.02 cm^2/ Vdet.

The change in density and charge carrier mobility is the contribution of the free electrons to indium tin oxide derived from the diffusion of the impurity atoms Sn^{+4} replacing the Sn^{+3} atom in the In_2O_3 parent grid according to equation (4). The electron contribution originating from Sn due to binding to oxygen replacing the position of the In atom on the In_2O_3 lattice

has a relation to the density of the load carrier which results in a change in electrical resistivity. The above mentioned changes are also caused by the electrons of free atoms In and Sn that are not able to oxidize due to the increased concentration of oxygen vacancies at the time of deposition. At the time of deposition, the In_2O_3 compound releases some oxygen, to a different composition initially that In_2O_{3-x} $(V_o'')_x e_{2x}$ with V_o'' denotes the oxygen vacuum of two electrons, whereas e_{2x}' represents the electron needed to be neutral. Similarly, from SnO_2 releasing some oxygen, it becomes a different composition initially that is SnO_{2-x} $(V_o'')_x e_{2x}'$ In general the thin film sample is estimated to be $In_{2-y}Sn_y'O_{3-x}$ $(V_o'')_x e_{2x}' e_y'$, Sn_y' substitution Sn to In which produces one free electron.

The oxidation conditions result in a change in the concentration of oxygen vacancies, and in turn can result in changes in load density. Increased oxygen content in the ITO layer can also improve the orientation of the carrier mobility. On the other hand the oxygen content may cause a change in the density of the load carrier and does not result in significant carrier mobility changes. The effect of increased oxygen density of insertion on grain boundaries and ћ∑ oxides is invisible.

Changes in the density and mobility of the carriers are due to several processes during the course of annealing, including oxygen absorption and diffusion of thin films. Due to the diffusion of oxygen can cause a decrease in oxygen vacuum. Annealing may cause diffusion of Sn impurity atoms from grain boundaries and lattice sites of insertions to normal lattice sites so Sn can act as an active donor because the atomic valence is greater than In. This annealing process improves the crystallinity or crystal growth process so as to minimize the scattering between the grain boundaries.

The change in electrical resistivity of the ITO layer after annealing is caused by the diffusion process of oxygen and the opposite diffusion of Sn. The oxygen diffusion causes the oxygen atoms to diffuse into the ITO thin films resulting in a decrease in the density of the oxygen vacuum during the annealing process whereas the diffusion Sn is the diffusion of Sn atoms from the grain boundary and the location of the insertion to the lattice location of In_2O_3 and form the SnO_2 oxide. Generally, donors from Sn are activated after experiencing a certain temperature increase so that the free electron density of the ITO thin layer increases in a certain temperature so that the free electron density of the ITO thin layer increases dramatically as shown in Fig. 6.

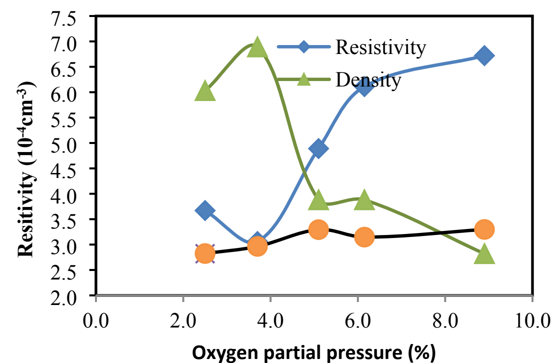

Fig. 6. Resistivity, density, mobility at annealing 250 ºC

The density decrease in oxygen partial pressure of 3.7% is due to the formation of InO, SnO and In and Sn free atoms capable of functioning as an impurities that act as centers of ion scattering.

Electrical resistivity decreased to 3.06 x 10^{-4} Ω cm in oxygen partial pressure 3.70% then increased to 6.72 x 10^{-4} Ω cm in oxygen partial pressure 3,70%-8,90%, and temperature annealing 250 ºC. The change in the density and mobility of the load carriers due to the oxygen void in In, is overcome when the addition of oxygen from the outside is 3.70%.

3.3 Optical Studies

Reflectance (R) is the ratio of the flux of reflected energy to the coming energy flux,

$$R = \frac{(n_2 - 1)^2 + k^2}{(n_2 + 1)^2 + k^2} \quad (7)$$

and the transmittance (T) thin films can be ignited with,

$$T = \left| \frac{2n_1}{n_2 + n_1} \right| \quad 8)$$

The relation of weakening index k with α absorption coefficient can be expressed by,

$$\alpha = \frac{4\pi k}{\lambda} \quad (9)$$

with α is the absorption coefficient, k index of attenuation bias and λ wavelength. Transmittance of electrons undergoing a direct transition [44],

$$\alpha h \upsilon \approx (h \upsilon - E_g)^n \quad (10)$$

with Eg is the bandgap of the transition energy band, the photon energy and n=1/2 for the direct transition and n = 3/2 for the indirect transition.

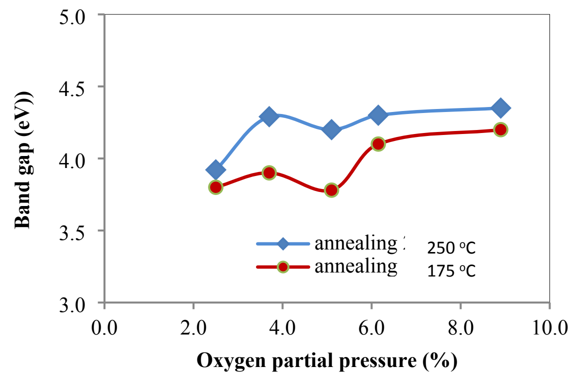

Fig. 7. Band gap energy ITO

Transmission changes to partial presure oxygen and annealing levels such as **Fig. 8.**

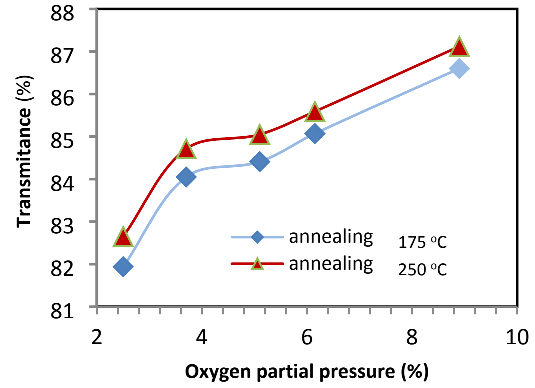

Fig. 8. ITO Transmittance.

The change in the bandgap of the ITO coating energy to changes in partial presuure oxygen and annealing such as **Fig. 7**. the energy band gap changes because the concentration of Sn dosing atoms starts to decrease due to the bonded Sn atom with oxygen added from the outside. So that the electron wave function at the level of impurities will not overlap each other. and affect the potential energy level changes of each electron which may result in the formation of a band of energy levels in the area. Another effect that arises as a consequence of the reduced concentration of impurities causes the lower energy band to expand, so that the band gap energy occurs tailings band effect.

The energy band gap shift can also be associated with the annealing temperature associated with the atom diffusion rate of oxygen at the grain boundary. A rise in partial pressure oxygen may increase **Fig.8** transmittance, as a result of the change of crystallination of thin layer of ITO FWHM increasing **Fig. 4**. ITO coated grains begin to leave the amorphous structure at temperature (150-250) °C to be fine grain with size between (68.99-122,76) nm.

The changing pattern of ITO layer transmittance to partial pressure oxygen and annealing changes such as **Fig. 8**. The high transmittance of some samples up to the area appears to correspond to the ITO material properties having a wide band of energy (3.78 - 4.35) eV.

The energy band gap shift due to vacancy was formulated by Burstein-Moss

[45] with, $E_g^{eff} = E_{go} + \Delta\sum_g^{BM} + \hbar\sum(k)$ where the electron scattering contribution is impurities. To reduce the contribution of electron impurities, In and Sn. The addition of partial pressure oxygen causes a decrease in electron impurities, so that the energy band gap widened [46-47].

Table 3 Optical parameter ITO thin films for different oxygen partial and annealing

Oxygen partial (%)	Annealing (^{o}C)	Wave lengh (nm)	Ref (%)	indeks bias	Peredaman constante (k)	coefient absorps (a)	Trans max (%)
2.50	175	686	11.96	2.18	3.30	0.061	81.94
	250	598	10.38	2.20	3.34	0.070	82.65
3.70	175	664	9.65	2.20	3.36	0.063	84.05
	250	615	8.39	2.18	3.36	0.069	84.71
5.10	175	591	8.40	2.20	3.38	0.072	84.41
	250	615	7.70	2.20	3.40	0.072	85.05
6.15	175	727	9.61	2.09	3.08	0.053	85.07
	250	664	10.76	2.22	1.93	0.036	85.59
8.90	175	668	7.00	2.22	3.44	0.065	86.60
-	250	700	6.61	2.25	3.49	0.062	87.12

4. Conclusions

The optimization of thin films of transparent ITO conductor is made by sputtering deposition technique to analyze structures, electrical properties and optical properties against parameters of partial oxygen pressure and annealing treatment, it can be concluded that prefared thin films are dominant in plane (400) and crystal levels, lattice constants, grain size changes with oxygen partial pressure and annealing changes. The electrical resistivity changed with the oxygen partial pressur and the annealing treatment, the most significant decrease of resistivity occurred in oxygen partial pressurre 3.70%. While the transmittance progresses to a larger oxygen partial pressurre, the transmittance is 87.12% at a temperature of 250 °C.

References

[1] A. Mavlonov *et al.*, “Superstrate-type flexible and bifacial Cu(In,Ga)Se2 thin-film solar cells with In2O3:SnO2 back contact,” *Solar Energy*, vol. 211, pp. 725–731, Nov. 2020, doi: 10.1016/j.solener.2020.10.019.

[2] Supriyono, H. Surahman, Y. K. Krisnandi, and J. Gunlazuardi, “Preparation and Characterization of Transparent Conductive SnO2-F Thin Film Deposited by Spray Pyrolysis: Relationship between Loading Level and Some Physical Properties,” *Procedia Environmental Sciences*, vol. 28, pp. 242–251, 2015, doi: 10.1016/j.proenv.2015.07.031.

[3] J. Zhang *et al.*, “Tailoring catalytic properties of V2O3 to propane dehydrogenation through single-atom doping: A DFT study,” *Catalysis Today*, p. S0920586120300754, Feb. 2020, doi: 10.1016/j.cattod.2020.02.023.

[4] M. Özdoğan, S. Yiğen, C. Çelebi, and G. Utlu, “The comparison of transient photocurrent spectroscopy measurements of Pulsed Electron Deposited ZnO thin film for air and vacuum ambient conditions,” *Thin Solid Films*, vol. 680, pp. 48–54, Jun. 2019, doi: 10.1016/j.tsf.2019.04.030.

[5] Y. Kwon *et al.*, “Control of oxidation behavior in high vacuum transmission electron microscopy,” *Materials Characterization*, vol. 172, p. 110870, Feb. 2021, doi: 10.1016/j.matchar.2020.110870.

[6] V. Gurylev and T. P. Perng, “Defect Engineering of ZnO: Review on Oxygen and Zinc Vacancies,” *Journal of the European Ceramic Society*, p. S0955221921001801, Mar. 2021, doi: 10.1016/j.jeurceramsoc.2021.03.031.

[7] K. C. Nwambaekwe *et al.*, “Crystal engineering and thin-film deposition strategies towards improving the performance of kesterite photovoltaic cell,” *Journal of Materials Research and Technology*, p. S223878542100274X, Mar. 2021, doi: 10.1016/j.jmrt.2021.03.047.

[8] A. S. A. C. Diniz and C. J. Kiely, “Crystallisation of indium-tin-oxide (ITO) thin films,” *Renewable Energy*, vol. 29, no. 13, pp. 2037–2051, Oct. 2004, doi: 10.1016/j.renene.2003.11.020.

[9] A. S. A. C. Diniz, “The effects of various annealing regimes on the microstructure and physical properties of ITO (In2O3:Sn) thin films deposited by electron beam evaporation for solar energy applications,” *Renewable Energy*, vol. 36, no. 4, pp. 1153–1165, Apr. 2011, doi: 10.1016/j.renene.2010.09.005.

[10] Y.-T. Li, D.-T. Chen, C.-F. Han, and J.-F. Lin, “Effect of the addition of zirconium on the electrical, optical, and mechanical properties and microstructure of ITO thin films,” *Vacuum*, vol. 183, p. 109844, Jan. 2021, doi: 10.1016/j.vacuum.2020.109844.

[11] S. Chapi, “Optical, electrical and electrochemical properties of PCL5/ITO transparent conductive films deposited by spin-coating – Materials for single-layer devices,” *Journal of Science: Advanced Materials and Devices*, vol. 5, no. 3, pp. 322–329, Sep. 2020, doi: 10.1016/j.jsamd.2020.07.005.

[12] Z. Yong *et al.*, “Ti1-Sn O2 nanofilms: Layer-by-layer deposition with extended Sn solubility and characterization,” *Applied Surface Science*, vol. 428, pp. 710–717, Jan. 2018, doi: 10.1016/j.apsusc.2017.09.135.

[13] N. A. Arifin, L. Troskialina, A. H. Shamsuddin, and R. Steinberger-Wilckens, “Effects of Sn doping on the manufacturing, performance and carbon deposition of Ni/ScSZ cells in solid oxide fuel cells,” *International Journal of Hydrogen Energy*, vol. 45, no. 51, pp. 27575–27586, Oct. 2020, doi: 10.1016/j.ijhydene.2020.07.071.

[14] C. Shang *et al.*, “Improving lithium storage capability of ternary Sn-based sulfides by enhancing inactive/active element ratio,” *Solid State Ionics*, vol. 337, pp. 47–55, Sep. 2019, doi: 10.1016/j.ssi.2019.04.008.

[15] M. Micali, S. Cosentino, and A. Terrasi, “Structural, optical and electrical characterization of ITO films co-doped with Molybdenum,” *Solar Energy Materials and Solar Cells*, vol. 221, p. 110904, Mar. 2021, doi: 10.1016/j.solmat.2020.110904.

[16] H. Zhu *et al.*, “Optical and electrical properties of ITO film on flexible fluorphlogopite substrate,” *Ceramics International*, p. S0272884221006556, Mar. 2021, doi: 10.1016/j.ceramint.2021.02.269.

[17] H. Wang *et al.*, “Influence of Ag incorporation on the structural, optical and electrical properties of ITO/Ag/ITO multilayers for inorganic all-solid-state electrochromic devices,” *Ceramics International*, vol. 47, no. 6, pp. 7666–7673, Mar. 2021, doi: 10.1016/j.ceramint.2020.11.109.

[18] M. Kumar, E.-C. Cho, M. F. Prodanov, C. Kang, A. K. Srivastava, and J. Yi, “MoOx work function, interface structure, and thermal stability analysis of ITO/MoOx/a-Si(i) stacks for hole-selective silicon heterojunction solar cells,” *Applied Surface Science*, vol. 553, p. 149552, Jul. 2021, doi: 10.1016/j.apsusc.2021.149552.

[19] N. Erdogan *et al.*, “ITO/Au/ITO multilayer thin films on transparent polycarbonate with enhanced EMI shielding properties,” *Current Applied Physics*, vol. 20, no. 4, pp. 489–497, Apr. 2020, doi: 10.1016/j.cap.2020.01.012.

[20] A. Mohamed Saleem, S. Gnanasaravanan, D. Saravanakkumar, S. Rajasekar, A. Ayeshamariam, and M. Jayachandran, “Preparation and characterization studies of TiO2 doped ZrO2 on ITO nanocomposites for optoelectronic applications,” *Materials Today:*

Proceedings, vol. 36, pp. 408–415, 2021, doi: 10.1016/j.matpr.2020.04.748.

[21] E. J. Herrera-Jimenez, E. Bousser, T. Schmitt, J. E. Klemberg-Sapieha, and L. Martinu, “Effect of plasma interface treatment on the microstructure, residual stress profile, and mechanical properties of PVD TiN coatings on Ti-6Al-4V substrates,” *Surface and Coatings Technology*, vol. 413, p. 127058, May 2021, doi: 10.1016/j.surfcoat.2021.127058.

[22] D. P. Pham *et al.*, “Control of preferred (222) crystalline orientation of sputtered indium tin oxide thin films,” *Thin Solid Films*, vol. 570, pp. 16–19, Nov. 2014, doi: 10.1016/j.tsf.2014.08.041.

[23] C. B. Silva, J. G. da Silva Filho, G. S. Pinheiro, A. M. R. Teixeira, F. F. de Sousa, and P. T. C. Freire, “High-pressure studies on l,l-dileucine crystals by Raman spectroscopy and synchrotron X-ray diffraction combined with DFT calculations,” *Spectrochimica Acta Part A: Molecular and Biomolecular Spectroscopy*, vol. 229, p. 117899, Mar. 2020, doi: 10.1016/j.saa.2019.117899.

[24] S. Y. P. Allain, S. Gaudez, G. Geandier, F. Danoix, M. Soler, and M. Goune, “Carbon heterogeneities in austenite during Quenching & Partitioning (Q&P) process revealed by in situ High Energy X-Ray Diffraction (HEXRD) experiments,” *Scripta Materialia*, vol. 181, pp. 108–114, May 2020, doi: 10.1016/j.scriptamat.2020.02.022.

[25] P. Shunmuga Sundaram, T. Sangeetha, S. Rajakarthihan, R. Vijayalaksmi, A. Elangovan, and G. Arivazhagan, “XRD structural studies on cobalt doped zinc oxide nanoparticles synthesized by coprecipitation method: Williamson-Hall and size-strain plot approaches,” *Physica B: Condensed Matter*, vol. 595, p. 412342, Oct. 2020, doi: 10.1016/j.physb.2020.412342.

[26] R. N. Chauhan and N. Tiwari, “Zinc oxide incorporated indium tungsten oxide amorphous thin films for thin film transistors applications,” *Journal of Non-Crystalline Solids*, vol. 556, p. 120556, Mar. 2021, doi: 10.1016/j.jnoncrysol.2020.120556.

[27] M. Simicic *et al.*, “Electrostatic discharge robustness of amorphous indium-gallium-zinc-oxide thin-film transistors,” *Microelectronics Reliability*, vol. 108, p. 113632, May 2020, doi: 10.1016/j.microrel.2020.113632.

[28] L. Fan *et al.*, “Crystal growth, finite element analysis and oxygen annealing of ZnO bulk crystal grown by low-temperature-gradient chemical vapor transport,” *Ceramics International*, vol. 46, no. 14, pp. 23107–23115, Oct. 2020, doi: 10.1016/j.ceramint.2020.06.088.

[29] M. Sobri *et al.*, “Effect of annealing on structural, optical, and electrical properties of nickel (Ni)/indium tin oxide (ITO) nanostructures prepared by RF magnetron sputtering,” *Superlattices and Microstructures*, vol. 70, pp. 82–90, Jun. 2014, doi: 10.1016/j.spmi.2014.02.010.

[30] R. N. Chauhan and N. Tiwari, “Preparation of optically transparent and conducting radio-frequency sputtered indium tin oxide ultrathin films,” *Thin Solid Films*, vol. 717, p. 138471, Jan. 2021, doi: 10.1016/j.tsf.2020.138471.

[31] S. Han, C. Hu, J. Yu, H. Jiang, and S. Wen, “Stabilization of inertial Cohen-Grossberg neural networks with generalized delays: A direct analysis approach,” *Chaos, Solitons & Fractals*, vol. 142, p. 110432, Jan. 2021, doi: 10.1016/j.chaos.2020.110432.

[32] K. Piler, C. Bahrim, S. Twagirayezu, and T. J. Benson, “Lattice disorders of TiO2 and their significance in the photocatalytic conversion of CO2,” in *Advances in Catalysis*, vol. 66, Elsevier, 2020, pp. 109–233.

[33] W. Fan, C. Liu, K. Gao, Y. Liang, and F. Liu, “Reconfigurable plasma photonic crystals from triangular lattice to square lattice in dielectric barrier discharge,” *Physics Letters A*, vol. 396, p. 127223, Apr. 2021, doi: 10.1016/j.physleta.2021.127223.

[34] J. Chen, J. Xie, E. Liu, B. Yan, and J. Liu, “Interface states in the rectangular lattice photonic crystals with identical dielectric rods,” *Results in Physics*, vol. 23, p. 104082, Apr. 2021, doi: 10.1016/j.rinp.2021.104082.

[35] F. J. Serrao, N. N. Bappalige, K. M. Sandeep, and S. Raghavendra, "Dominance of c-axis orientation on the carrier transport properties of Sn doped ZnO thin films," *Thin Solid Films*, vol. 722, p. 138579, Mar. 2021, doi: 10.1016/j.tsf.2021.138579.

[36] M. Alzaid, "Tailoring the thermoelectric properties of bulk ZnAlO with different aluminum concentrations (1, 1.5 and 2%) by post annealing in air at various temperatures," *Physica B: Condensed Matter*, vol. 603, p. 412727, Feb. 2021, doi: 10.1016/j.physb.2020.412727.

[37] X. Zhang, M. Liu, H. Sun, and J. Banhart, "Influence of Sn on the age hardening behavior of Al–Mg–Si alloys at different temperatures," *Materialia*, vol. 8, p. 100441, Dec. 2019, doi: 10.1016/j.mtla.2019.100441.

[38] O. V. Shiman, L. Balogh, and M. R. Daymond, "A synchrotron X-ray diffraction study of strain and microstrain distributions in α-Zr caused by hydride precipitation," *Surfaces and Interfaces*, vol. 17, p. 100388, Dec. 2019, doi: 10.1016/j.surfin.2019.100388.

[39] A. J. Goodfellow, J. Kelleher, N. G. Jones, D. Dye, M. C. Hardy, and H. J. Stone, "The effect of Mo on load partitioning and microstrain evolution during compression of a series of polycrystalline Ni-Based superalloys," *Acta Materialia*, vol. 176, pp. 318–329, Sep. 2019, doi: 10.1016/j.actamat.2019.07.002.

[40] A. Nikiforov *et al.*, "Formation of SnO and SnO2 phases during the annealing of SnO(x) films obtained by molecular beam epitaxy," *Applied Surface Science*, vol. 512, p. 145735, May 2020, doi: 10.1016/j.apsusc.2020.145735.

[41] Z. Wang *et al.*, "SnO-SnO2 modified two-dimensional MXene Ti3C2T for acetone gas sensor working at room temperature," *Journal of Materials Science & Technology*, vol. 73, pp. 128–138, May 2021, doi: 10.1016/j.jmst.2020.07.040.

[42] H. Lv *et al.*, "Two-dimensional SnO/SnO2 heterojunctions for electromagnetic wave absorption," *Chemical Engineering Journal*, vol. 411, p. 128445, May 2021, doi: 10.1016/j.cej.2021.128445.

[43] S. Gambino, "The impact of charge carrier relaxation, electron trapping and oxygen p-doping on the photocurrent transients of a conjugated polymer probed by the Time of Flight method," *Thin Solid Films*, vol. 718, p. 138485, Jan. 2021, doi: 10.1016/j.tsf.2020.138485.

[44] S. Y. Lee, E.-S. Cho, and S. J. Kwon, "The optical analyses of the multilayer transparent electrode and the formation of ITO/Mesh-Ag/ITO multilayers for enhancing an optical transmittance," *Applied Surface Science*, vol. 487, pp. 990–999, Sep. 2019, doi: 10.1016/j.apsusc.2019.05.106.

[45] A. Khan, F. Rahman, R. Nongjai, and K. Asokan, "Structural, optical and electrical transport properties of Sn doped In2O3," *Solid State Sciences*, vol. 109, p. 106436, Nov. 2020, doi: 10.1016/j.solidstatesciences.2020.106436.

[46] G. Manjunatha, C. Rajashekhar, K. V. Prasad, H. Vaidya, and Saraswati, "Peristaltic flow of a Jeffery fluid over a porous conduit in the presence of variable liquid properties and convective boundary conditions," *International Journal of Thermofluid Science and Technology*, vol. 6, no. 2, Nov. 2019, doi: 10.36963/IJTST.19060201.

[47] H. Vaidya, K. V. Prasad, K. Vajravelu, C.-O. Ng, S. Nadeem, and U. B. Vishwanatha, "The Effects of Thermocapillarity on the Thin Film Flow of MHD UCM Fluid over an Unsteady Elastic Surface with Convective Boundary Conditions," *International Journal of Thermofluid Science and Technology*, vol. 6, no. 3, Nov. 2019, doi: 10.36963/IJTST.19060303.